

Chiral symmetry restoration by parity doubling and the structure of neutron stars

Michał Marczenko,¹ David Blaschke,^{1,2,3} Krzysztof Redlich,^{1,4} and Chihiro Sasaki¹

¹*Institute of Theoretical Physics, University of Wrocław, PL-50204 Wrocław, Poland*

²*Bogoliubov Laboratory of Theoretical Physics, Joint Institute for Nuclear Research, 141980 Dubna, Russia*

³*National Research Nuclear University, 115409 Moscow, Russia*

⁴*Extreme Matter Institute EMMI, GSI, D-64291 Darmstadt, Germany*

(Dated: December 14, 2024)

We investigate the equation of state for the recently developed hybrid quark-meson-nucleon model under neutron star conditions of β -equilibrium and charge neutrality. The model has the characteristic feature that, at increasing baryon density, the chiral symmetry is restored within the hadronic phase by lifting the mass splitting between chiral partner states, before quark deconfinement takes place. Most important for this study are the nucleon (neutron, proton) and $N(1535)$ states. We present different sets for two free parameters, which result in compact star mass-radius relations in accordance with modern constraints on the mass from PSR J0437-4715 and on the compactness from GW170817. We also consider the threshold for the direct URCA process for which a new relationship is given, and suggest as an additional constraint on the parameter choice of the model that this process shall become operative at best for stars with masses above the range for binary radio pulsars, $M > 1.4 M_\odot$.

I. INTRODUCTION

The investigation of the equation of state (EoS) of compact star matter became rather topical within the past few years, mainly due to the one-to-one correspondence between EoS and mass-radius (M-R) relationship [1] for the corresponding sequence of compact stars via the solution of the Tolman-Oppenheimer-Volkoff (TOV) equations [2, 3]. Masses and radii of pulsars are target of observational programs, which can therefore provide stringent constraints to the EoS and phase structure of quantum chromodynamics (QCD) in a region of the QCD phase diagram that is inaccessible to terrestrial experiments and present techniques of lattice QCD simulations. For the extraction of the compact star EoS via Bayesian analysis techniques using mass and radius measurements as priors see Refs. [4–6]. In particular, in the era of multi-messenger astronomy, it shall soon become possible to constrain the sequence of stable compact star configurations in the mass-radius plane inasmuch that a benchmark for the EoS of cold and dense matter can be deduced from it. This would play a similar role for the development of effective models of the QCD phase structure as the ab-initio calculations of lattice QCD at finite temperature and vanishing baryon density [7].

In the study of cold and dense QCD and its applications, commonly used are separate effective models for the nuclear and quark matter phases (two-phase approaches) with a priori assumed first-order phase transition, typically associated with simultaneous chiral and deconfinement transitions. Within this setting, for a constant-speed-of-sound (CSS) model of high-density (quark) matter, a systematic classification of hybrid compact star solutions has been given in [8], which gives a possibility to identify a strong first-order transition in the EoS by the fact that the hybrid star branch in the M-R diagram becomes disconnected from the branch of pure neutron stars. However, already before this occurs, a

strong phase transition manifests itself by the appearance of an almost horizontal branch on which the hybrid star solutions lie, as opposed to the merely vertical branch of pure neutron stars. In the literature, this strong phase transition has been discussed as due to quark deconfinement [9]. This conclusion, as we shall demonstrate in this work, may however be premature since strong phase transitions with a large latent heat occur also within hadronic matter, for instance due to the onset of Δ -matter [10] or just the chiral restoration transition inside the nuclear matter phase, which we discuss here.

In this work, we explore the implications of dynamical sequential phase transitions at high baryon density on the structure of neutron stars. To this end, we employ the hybrid quark-meson-nucleon (QMN) model [11, 12] and extend it by including the isovector ρ meson. We demonstrate how high-mass star configurations can be achieved with different neutron-star interior. We find that, depending on the parametrization, the model predicts different stable configurations with similar mass $M \simeq 2 M_\odot$. Our main focus is on the role of the chiral symmetry restoration in the high-mass part of the mass-radius sequence.

In the model parametrization, we pay special attention to recent observational constraints from neutron star physics, in particular from the precise measurement of the high mass $2.01(4) M_\odot$ for PSR J0348+432 [13], and for the compactness constraint at $M = 1.4 M_\odot$ from the gravitational wave detection of the inspiral phase of the binary neutron star merger GW170817 [14], which constrains the radius at this mass to 13.6 km [15]. Furthermore, we consider the so-called "direct URCA constraint" for the cooling of compact stars which gives a constraint on the admissible proton fraction in typical-mass compact stars (see, e.g., Ref. [16]).

This paper is organized as follows. In Sec. II, we introduce the hybrid quark-meson-nucleon model, as well as its extension to arbitrary isospin. In Sec. III, we dis-

cuss the obtained numerical results on the equation of state under the neutron-star conditions. In Sec. IV, we discuss the obtained neutron-star relations, the direct URCA process, the tidal deformability, as well as possible realizations of QCD. Finally, Sec. V is devoted to summary and conclusions.

II. HYBRID QUARK-MESON-NUCLEON MODEL

In this section, we briefly introduce the hybrid quark-meson-nucleon (QMN) model for the QCD transitions at finite temperature and density [11, 12] for the isospin-symmetric matter, and extend it to an arbitrary isospin for the application to the physics of neutron stars.

The hybrid QMN model is composed of the baryonic parity-doublers [17–19] and mesons as in the Walecka model, as well as quark degrees of freedom as in the standard quark-meson model. The spontaneous chiral symmetry breaking yields the mass splitting between the two baryonic parity partners, while it generates entire mass of a quark. In this work, we consider a system with $N_f = 2$, hence, relevant for this study are the lowest nucleons and their chiral partners, as well as the up and down quarks. The hadronic degrees of freedom are coupled to the chiral fields (σ , π), and the iso-singlet vector field ω_μ , while the quarks are coupled solely to the former. Another important feature of the hybrid QMN model is that it realizes the concept of statistical confinement by taking into account a medium-dependent modification of the distribution functions, where an additional real scalar field b is introduced.

In the mean-field approximation, the thermodynamic potential of the hybrid QMN model reads^{#1}

$$\Omega = \sum_x \Omega_x + V_\sigma + V_\omega + V_b, \quad (1)$$

where the summation in the first term goes over the up (u) and down (d) quarks, as well as the nucleonic states with positive and negative parity. The positive-parity nucleons correspond to the positively charged and neutral $N(938)$ states, i.e., proton (p_+) and neutron (n_+), respectively. The negative-parity nucleons are identified as their counterparts, $N(1535)$ [20], and are denoted as p_- and n_- . The kinetic term, Ω_x , reads

$$\Omega_x = \gamma_x \int \frac{d^3p}{(2\pi)^3} T [\ln(1 - n_x) + \ln(1 - \bar{n}_x)]. \quad (2)$$

^{#1} We note that the original hybrid QMN model deals with conformal anomaly as well [11]. However, the presence of the dilaton (glueball) does not affect the nuclear groundstate properties in the mean-field approximation due to its heavy mass. Moreover, its expectation value is almost constant in the region of our interest. Hence, following our previous work [12], we do not take the dilaton dynamics into account.

The factor $\gamma_\pm = 2$ denotes the spin degeneracy for the nucleons with positive/negative parity, and $\gamma_q = 2 \times 3 = 6$ is the spin-color degeneracy factor for the quarks. The functions n_x are the modified Fermi-Dirac distribution functions for the nucleons

$$\begin{aligned} n_\pm &= \theta(\alpha^2 b^2 - \mathbf{p}^2) f_\pm, \\ \bar{n}_\pm &= \theta(\alpha^2 b^2 - \mathbf{p}^2) \bar{f}_\pm, \end{aligned} \quad (3)$$

and for the quarks, accordingly

$$\begin{aligned} n_q &= \theta(\mathbf{p}^2 - b^2) f_q, \\ \bar{n}_q &= \theta(\mathbf{p}^2 - b^2) \bar{f}_q, \end{aligned} \quad (4)$$

where b is the expectation value of the b -field, and α is a dimensionless model parameter [11, 12]. From the definition of n_\pm and n_q , it is evident that, to mimic the statistical confinement, the expected behavior of the b field is to have a non-trivial vacuum expectation value, in order to favor the hadronic degrees of freedom over the quark ones at low densities. On the other hand, it is expected that it vanishes at higher densities in order to suppress the hadronic degrees of freedom and to allow for the population of quarks. This is achieved by allowing b to be generated from a potential V_b (to be introduced later in this section). The functions f_x and \bar{f}_x are the standard Fermi-Dirac distributions,

$$\begin{aligned} f_x &= \frac{1}{1 + e^{\beta(E_x - \mu_x)}}, \\ \bar{f}_x &= \frac{1}{1 + e^{\beta(E_x + \mu_x)}}, \end{aligned} \quad (5)$$

with β being the inverse temperature, the dispersion relation $E_x = \sqrt{\mathbf{p}^2 + m_x^2}$. The effective chemical potentials for p_\pm and n_\pm are defined as^{#2}

$$\begin{aligned} \mu_{p_\pm} &= \mu_B - g_\omega \omega + \mu_Q, \\ \mu_{n_\pm} &= \mu_B - g_\omega \omega. \end{aligned} \quad (6)$$

The constant g_ω couples the nucleons to the ω field. Its strength is fixed by the nuclear saturation properties [11, 12]. The effective chemical potentials for up and down quarks are given by

$$\begin{aligned} \mu_u &= \frac{1}{3}\mu_B + \frac{2}{3}\mu_Q, \\ \mu_d &= \frac{1}{3}\mu_B - \frac{1}{3}\mu_Q. \end{aligned} \quad (7)$$

In Eqs. (6) and (7), μ_B , μ_Q are the baryon and charge chemical potentials, respectively. The effective masses of the parity doublers $m_{p_\pm} = m_{n_\pm} \equiv m_\pm$, are given by

$$m_\pm = \frac{1}{2} \left[\sqrt{(g_1 + g_2)^2 \sigma^2 + 4m_0^2} \mp (g_1 - g_2) \sigma \right], \quad (8)$$

^{#2} In the mean-field approximation, the non-vanishing expectation value of the ω field is the time-like component, hence we simply denote it by $\omega_0 \equiv \omega$.

m_0 [MeV]	m_σ [MeV]	g_ω	g_ρ	g_1	g_2	g_q	κ_b [MeV]	λ_b
790	370.58	6.80	7.98	13.00	6.96	3.36	155	0.074
800	363.68	6.54	8.00					
820	348.68	6.00	8.06					
840	313.83	5.44	8.11					

TABLE I. Sets of the model parameters used in this work. The values of m_σ and g_ω are fixed by the nuclear groundstate properties (see Ref. [12]), while g_ρ by the symmetry energy (see text). The remaining parameters do not depend on the choice of m_0 , and their values are taken from Ref. [12]

and for quarks, $m_u = m_d \equiv m_q$,

$$m_q = g_\sigma \sigma. \quad (9)$$

The parameters g_1 , g_2 , g_σ are Yukawa-coupling constants, m_0 is the chirally invariant mass of the baryons and is treated as an external parameter (for more details, see Ref. [12]). The values of those couplings can be determined by fixing the fermion masses. We take the vacuum masses of the positive- and negative-parity hadronic states to be $m_+ = 939$ MeV, $m_- = 1500$ MeV, respectively. The quark mass is assumed to be $m_+ = 3m_q$ in the vacuum. When the chiral symmetry is restored, the masses of the baryonic parity partners become degenerate with a common finite mass $m_\pm (\sigma = 0) = m_0$, which reflects the parity doubling structure of the low-lying baryons. This is in contrast to the quarks, which become massless as the chiral symmetry gets restored.

The potentials in Eq. (1) are as in the ordinary SU(2) linear sigma model,

$$V_\sigma = -\frac{\lambda_2}{2} (\sigma^2 + \pi^2) + \frac{\lambda_4}{4} (\sigma^2 + \pi^2)^2 - \epsilon \sigma, \quad (10a)$$

$$V_\omega = -\frac{1}{2} m_\omega^2 \omega_\mu \omega^\mu, \quad (10b)$$

$$V_b = -\frac{1}{2} \kappa_b^2 b^2 + \frac{1}{4} \lambda_b b^4, \quad (10c)$$

where the parameters λ_2 , λ_4 , and ϵ are

$$\lambda_2 = \frac{m_\sigma^2 - 3m_\pi^2}{2}, \quad \lambda_4 = \frac{m_\sigma^2 - m_\pi^2}{2f_\pi^2}, \quad \epsilon = m_\pi^2 f_\pi, \quad (11)$$

where the pion mass $m_\pi = 138$ MeV, pion decay constant $f_\pi = 93$ MeV. The sigma mass, m_σ , is treated as an external parameter, and is fixed by the properties of the nuclear groundstate. The constants κ_b and λ_b are fixed following Ref. [11].

In this work, in order to study matter under neutron star conditions, we extend the hybrid QMN model to the case of arbitrary isospin asymmetry. To this end, we introduce an additional term to the Lagrangian density for symmetric matter together with a Yukawa coupling to the isovector ρ meson field [21], namely

$$\mathcal{L}_\rho = -\frac{1}{2} g_\rho \sum_{k=1,2} \bar{\psi}_k \boldsymbol{\tau} \cdot \boldsymbol{\rho} \psi_k - \frac{1}{4} \boldsymbol{\rho}_{\mu\nu} \cdot \boldsymbol{\rho}^{\mu\nu} - V_\rho, \quad (12)$$

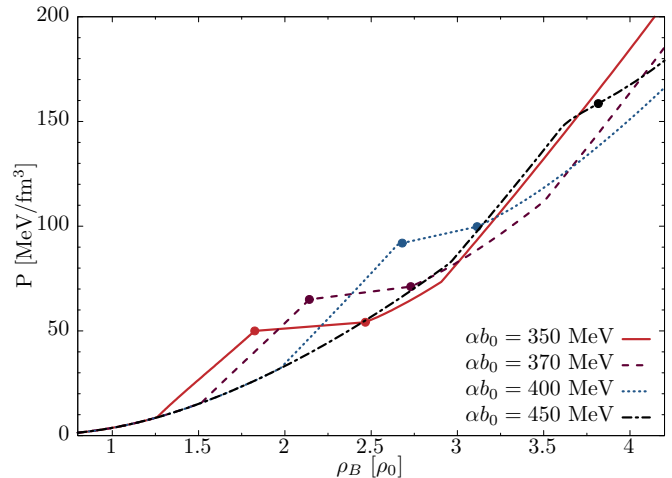


FIG. 1. Thermodynamic pressure P as a function of the net-baryon number density ρ_B , in units of the saturation density, $\rho_0 = 0.16 \text{ fm}^{-3}$. The regions between circles correspond to the coexistence of chirally broken and restored phases in the first-order phase transition. For $\alpha b_0 = 450$ MeV the transition is a crossover. The deconfinement transitions are triggered at higher densities and are not shown here.

where ψ_k is a set of the the baryonic chiral fields. The term $\boldsymbol{\rho}^{\mu\nu} = \partial^\mu \boldsymbol{\rho}^\nu - \partial^\nu \boldsymbol{\rho}^\mu - g_\rho \boldsymbol{\rho}^\mu \times \boldsymbol{\rho}^\nu$ is the field-strength tensor of the isovector field, and the mass term

$$V_\rho = -\frac{1}{2} m_\rho^2 \boldsymbol{\rho}_\mu \boldsymbol{\rho}^\mu, \quad (13)$$

with m_ρ being the mass of the ρ meson.

Taking the extension from Eq. (12) into account, the mean-field thermodynamic potential is obtained as

$$\Omega = \sum_x \Omega_x + V_\sigma + V_\omega + V_b + V_\rho. \quad (14)$$

Due to the inclusion of the ρ meson, the effective chemical

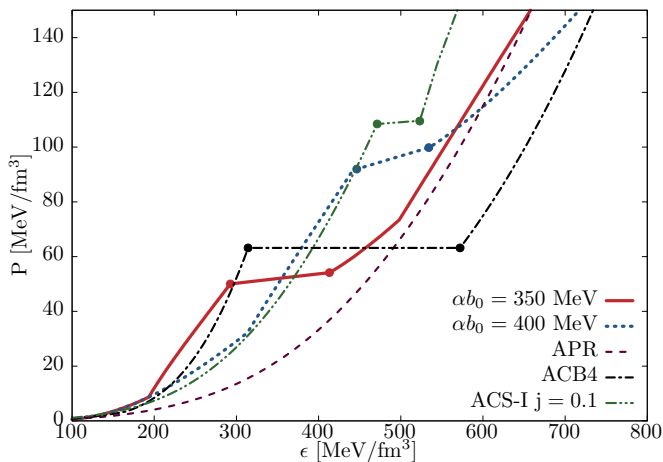


FIG. 2. Thermodynamic pressure P as a function of the energy density ϵ for two parametrizations of the hybrid QMN model. For comparison, shown are also three EoS from Ref. [22]: (i) the APR EoS (purple dashed line) (ii) the multipolytrope EoS labeled ACB4 (black dash-dotted line), as well as (iii) the hybrid EoS ACS-I (green dash-doubly-dotted line).

potentials (6) now become^{#3},

$$\begin{aligned}\mu_{p\pm} &= \mu_B - g_\omega\omega - \frac{1}{2}g_\rho\rho + \mu_Q, \\ \mu_{n\pm} &= \mu_B - g_\omega\omega + \frac{1}{2}g_\rho\rho.\end{aligned}\quad (15)$$

In the quark sector, a coupling of quarks to the ρ mean field in principle can also be introduced. However, since we do not reach any consensus about its nature yet, we turn it off in the current work in order to avoid unnecessary complexity and to reduce the number of free parameters. As a result of this assumption, the effective chemical potentials for quarks given in Eq. (7) remain unaffected.

The inclusion of the isovector field as in Eq. (12) introduces two additional parameters, i.e., the vacuum mass of the ρ meson, m_ρ and the coupling, g_ρ . The former is set to be $m_\rho = 775$ MeV [20], while the value of the latter can be fixed by fitting the value of symmetry energy, $E_{\text{sym}} = 31$ MeV [23]. The precise strength of the coupling depends on the value of the chirally invariant mass m_0 . Following the previous studies of the parity-doublet-based models [11, 12, 24], as well as recent lattice QCD results [25, 26], we choose rather large values, $m_0 = 790, 800, 820, 840$ MeV. The model parameters to be used in this work are summarized in Table I. In-medium profiles of the mean fields are obtained by extremizing the thermodynamic potential (14).

^{#3} We denote the non-vanishing component, time-like and neutral, by $\rho_{03} \equiv \rho$, just like the ω .

Several approaches with parity doubling of baryons exist and have been applied to in-medium QCD and neutron stars [27–34]. A different class of quark-hadron hybrid models [33, 34] includes Polyakov loop to thermally suppress quarks in hadronic phase. At finite temperature and small chemical potential, the center of SU(3) gauge group, Z(3) symmetry, may still be useful to guide the physics of deconfinement to some extent. Under the neutron star conditions, however, the explicit breaking of the Z(3) symmetry is no longer soft, so that it is conceptually questionable to start with this symmetry to constraint any effective Lagrangian. Our hybrid approach is superior in this context to the approaches with the Polyakov loop.

In the next section we discuss the influence of the external parameter α on the equation of state in the hybrid QMN model and its impact on the chiral phase transition, under the neutron-star conditions of β equilibrium and charge neutrality.

III. EQUATION OF STATE

The composition of neutron star matter requires β equilibrium, as well as the charge neutrality condition. To this end, we include electrons and muons as gases of free relativistic particles. In Fig. 1, we show the calculated zero-temperature equations of state in the mean-field approximation with $m_0 = 790$ MeV, for different values of the α parameter, namely $\alpha b_0 = 350$ MeV (solid red line), $\alpha b_0 = 370$ MeV (dashed magenta line), $\alpha b_0 = 400$ MeV (dotted blue line) and $\alpha b_0 = 450$ MeV (dash-dotted black line). The value b_0 is the vacuum expectation value of the b -field. The mixed phases of the chirally broken and restored phases are shown between circles. We stress that the chiral and hadron-to-quark phase transitions are sequential. The latter happen at higher densities and are not shown in the figure.

In all cases, the low-density behavior is similar. In the case of $\alpha b_0 = 350$ MeV, the chiral phase transition is triggered at roughly $1.82 \rho_0$, with the mixed phase persisting up to $2.46 \rho_0$. Higher values of α parameter yield weaker transitions at higher densities. For $\alpha b_0 = 370$ MeV, the mixed phase appears between $2.14 - 2.73 \rho_0$, and for $\alpha b_0 = 400$ MeV between $2.68 - 3.11 \rho_0$. On the other hand, for $\alpha b_0 = 450$ MeV, the transition turns into a crossover at roughly $3.81 \rho_0$. This stays in correspondence to the case of isospin-symmetric matter, where higher value of α weakens the first-order chiral phase transition, which goes through a critical point, and eventually turns into a crossover transition [12].

We stress that since the equations of state are derived by extremizing the thermodynamic potential of Eq. (14) with respect to the four mean fields, they are thermodynamically consistent and preserve causality, hence $c_s^2 \leq 1$.

For comparison, in Fig. 2, we show the pressure as a function of the energy density for $\alpha b_0 = 350, 400$ MeV together with the APR EoS [35] (purple dashed line),

which is a standard EoS used in astrophysics of compact stars, their mergers, as well as supernovae. The APR EoS shows similar high-density behavior, while being softer in the low-density part, just above the saturation density. Also shown are two EoS taken from Ref. [22], the multi-polytrope EoS ACB4 (black dash-dotted line), which features a strong first-order phase transition and produces high-mass twin star configurations, as well as the hybrid EoS ACS-1 (green dashed-doubly-dotted line) with a phase transition to constant-speed-of-sound matter at high density.

All the EoS shown in Fig. 2 fall into the region derived in [36] from the maximum mass constraint $M_{\max} \geq 2.01(4) M_{\odot}$ [13] using a multi-polytrope ansatz for the EoS at supersaturation densities (see also [37]). We like to note that the stiffening effect of nuclear matter just above the saturation density when compared to the non-relativistic APR EoS is a feature which the present approach has in common with the relativistic density-functional models of nuclear matter underlying the ACB [37] and ACS [38] class of EoS. The extreme stiffening in the case of $\alpha b_0 = 350$ MeV and for ACB4 (here due to a nucleonic excluded volume) is at certain tension with the recent analysis of GW170817 by Annala *et al* [15]. This tension could be resolved, e.g., by a strong phase transition occurring in the compact star mass range relevant for GW170817 (see Ref. [22]).

IV. RESULTS

A. TOV solutions for compact star sequences

We use the equations of state introduced in the previous section (see Fig. 1) to solve the general-relativistic Tolman–Oppenheimer–Volkoff (TOV) equations [2, 3] for spherically symmetric objects,

$$\frac{dP(r)}{dr} = -\frac{(\epsilon(r) + P(r))(M(r) + 4\pi r^3 P(r))}{r(r - 2M(r))}, \quad (16a)$$

$$\frac{dM(r)}{dr} = 4\pi r^2 \epsilon(r), \quad (16b)$$

with the boundary conditions $P(r=R) = 0$, $M = M(r=R)$, where R and M are the radius and the mass of a neutron star, respectively. Once the initial conditions are specified based on a given equation of state, namely the central pressure P_c and the central energy density ϵ_c , the internal profile of a neutron star can be calculated.

In Fig. 3, we show the relationship of mass versus central net-baryon density, for the calculated sequences of compact stars, together with the state-of-the-art constraint on the maximum mass for the pulsar PSR J0348-0432 [13]. We like to point out that the chiral restoration transition leads to a softening of the EoS so that it is accompanied by a strong increase of the central densities, while the mass of the star is almost unchanged.

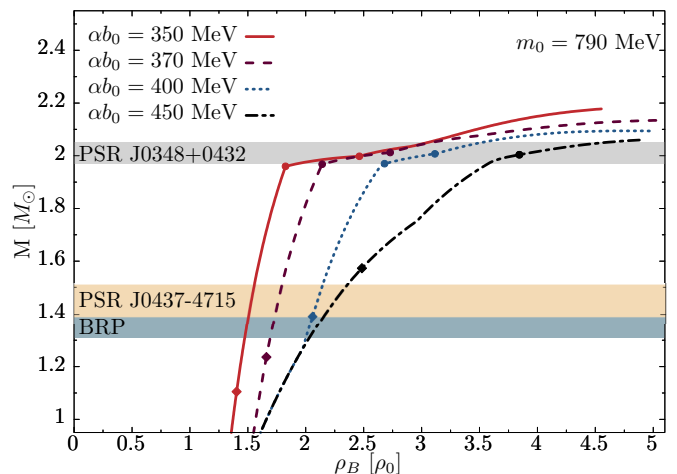


FIG. 3. Sequences of masses for compact stars vs. their central net-baryon density as solutions of the TOV equations for $m_0 = 790$ MeV and four different cases of $\alpha b_0 = 350, 370, 400, 450$ MeV. The regions between the circles show the coexistence of the chirally broken and chirally restored phases. The diamonds indicate the threshold mass for the direct URCA process (see Sec. IV B). The upper gray band is the $2.01(4) M_{\odot}$ observational constraint [13], the orange band, $1.44(7) M_{\odot}$, shows the mass of PSR J0437-4715 for which the NICER experiment [39] will soon provide a radius measurement [40]. Finally, the lower blue band is the $1.35(4) M_{\odot}$ binary radio pulsar (BRP) constraint [41].

In general, there is one-to-one correspondence between an EoS and the mass-radius relation calculated with it. The three curves for $\alpha b_0 = 350, 370, 400$ MeV consist of three phases; the chirally broken phase in the low-mass part of the sequence, the chirally restored phase in the high-mass part, and the mixed phase between filled circles. Similarly to the equation of state, increasing the value of α softens the chiral transition, which eventually becomes a smooth crossover for $\alpha b_0 = 450$ MeV and consists only of branches with chiral symmetry being broken and restored, separated by a circle. We note that the end points of the lines correspond to the onset of quark degrees of freedom in each case, after which the equation of state is not stiff enough to sustain the gravitational collapse and the branches become immediately unstable. This is because, in the current model setup, quarks are not coupled with the vector field leading to a repulsive force. On the other hand, it is known that repulsive interactions tend to stiffen the equation of state. Hence, an additional repulsive force in the quark sector could possibly make the branch stiff enough, so that an additional family of stable hybrid compact stars would appear, with the possibility for the high-mass twin scenario advocated by other effective models [37, 42, 43]. We leave a further study of quark matter as our future work.

Notably, the chiral transition for all values of αb_0 occurs in the high-mass part of the sequence, namely in the vicinity of the $2 M_{\odot}$ constraint, followed by a rapid

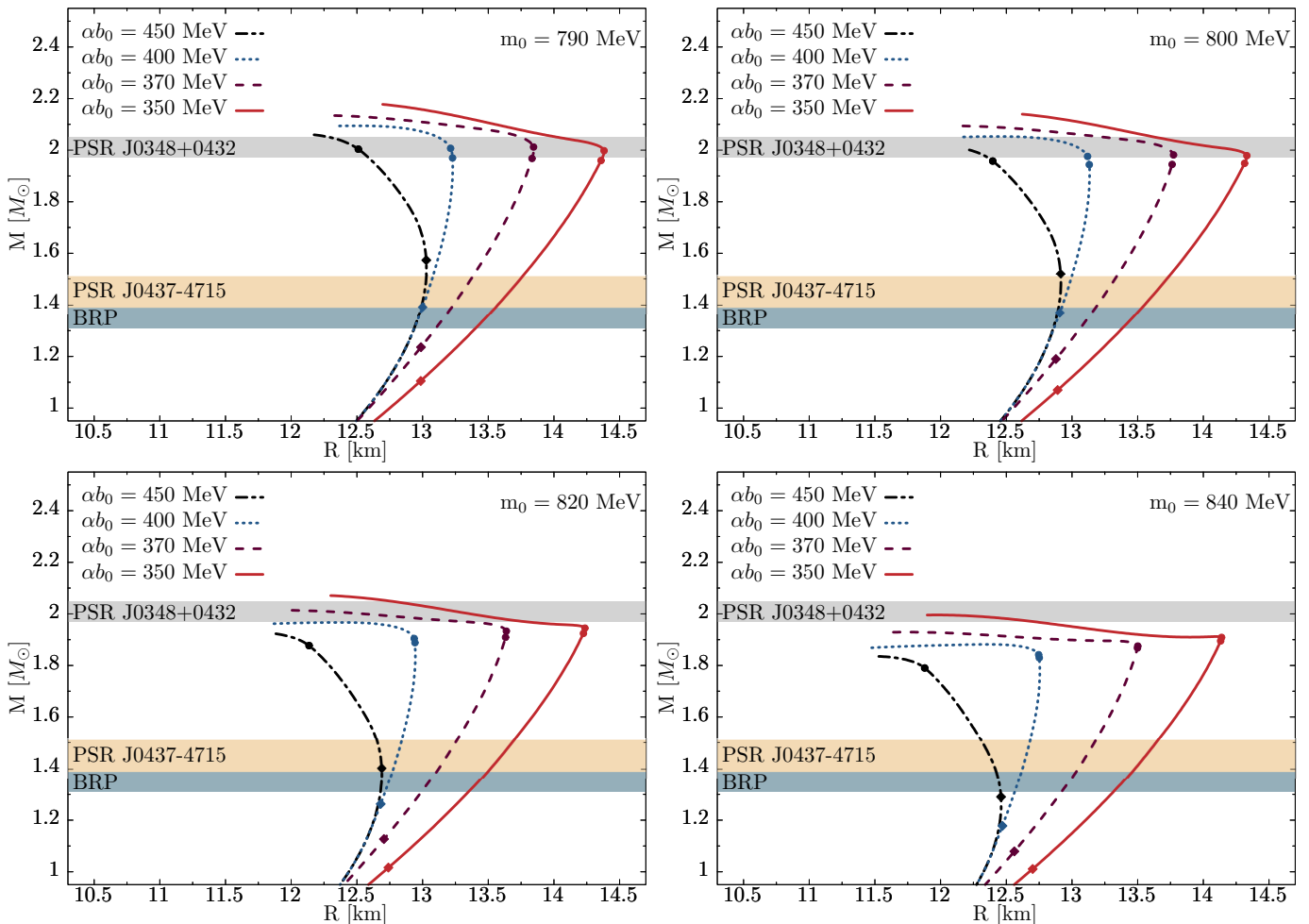


FIG. 4. Mass-radius sequences for $m_0 = 790$ MeV (upper left), $m_0 = 800$ MeV (upper right), $m_0 = 820$ MeV (lower left) and $m_0 = 840$ MeV (lower right), where the legend of the curves as well as the meaning of the circles and diamonds is the same as in Fig. 3.

flattening of the mass-radius sequence. The transitions are, however, not strong enough to produce an additional family of solutions, disconnected by an unstable branch.

In the upper left panel of Fig. 4, we show the mass-radius relations for the case $m_0 = 790$ MeV. In the three remaining panels, we show mass-radius relations obtained for different values of the chirally invariant mass m_0 . What is evident is that, increasing the value of m_0 systematically strengthens the chiral phase transition. This is seen twofold, as a shrinking of the mixed phases, as well as more abrupt flattening of chirally restored branches. For a larger m_0 the transition becomes strong enough to produce disconnected branches (see, e.g., the red solid line in the bottom right panel of Fig. 4). These, in turn, cause the maximal mass of the mass-radius sequences to decrease with increasing value of m_0 . Eventually, the equations of state become not stiff enough to reach the $2 M_\odot$ constraint. We note that the obtained mass-radius relations stay in good agreement with the low-mass constraints derived from the recent neutron-

star merger, namely that the radius of a $1.6 M_\odot$ neutron star must be larger than $10.68^{+0.15}_{-0.04}$ km [44].

In Fig. 5, we show the energy density profiles of stars for $m_0 = 790$ MeV. The bottom panel shows profiles of stars with mass $M = 1.97 M_\odot$. The cases with $\alpha b_0 = 400$ and 450 MeV show the profiles, which interiors consist only of nuclear matter with broken chiral symmetry (green region). For the stars with $\alpha b_0 = 350$ and 370 MeV, the chiral transitions are triggered at roughly 1.2 and 0.4 km radii, respectively, and, in their cores only the mixed phase (blue region) is realized. The radii of these stars vary from 13.7 km to 14.3 km. In the top panel, we show profiles of stars with mass $M = 2.05 M_\odot$. The chiral transitions are triggered in all four cases, and the chirally restored phase is reached in their cores (red region). For $\alpha b_0 = 350$ MeV, the mixed phase is featured between $5.3 - 5.8$ km radius, for $\alpha b_0 = 370$ MeV between $3.6 - 4.4$ km, for $\alpha b_0 = 400$ MeV between $3.3 - 4.1$ km. For $\alpha b_0 = 450$ MeV, as discussed in previous sections, the transition is a smooth crossover. In this case, we as-

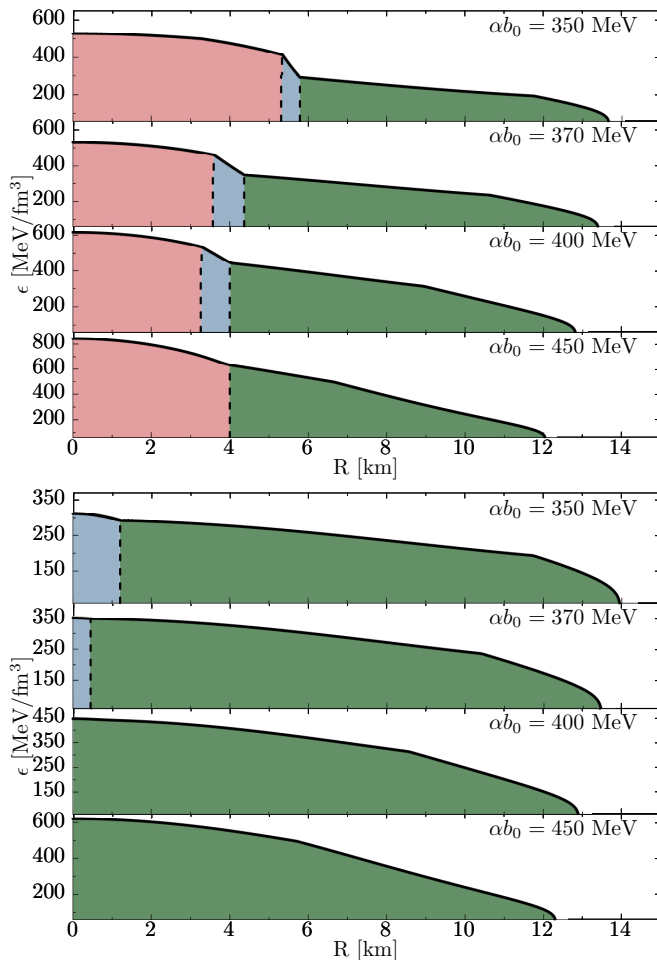


FIG. 5. Profiles of the energy density for neutron stars with $M = 1.97 M_\odot$ (bottom panel) and $M = 2.05 M_\odot$ (top panel) for $m_0 = 790$ MeV, for four different cases $\alpha b_0 = 350, 370, 400, 450$ MeV. The green regions show the phase, where the chiral symmetry is broken, in the red regions chiral symmetry is restored, whereas the blue regions indicate the regions of coexistence of both phases (mixed phase).

sume the chirally broken and chirally restored phases are separated by the peak in $\partial\sigma/\partial\mu_B$, which happens around 4.0 km radius. The radii of these stars vary from 12.2 km to 14.0 km.

In Fig. 6 we show the composition of compact star matter as a function of the baryon density for the present model. The chirally invariant mass of baryons is fixed to $m_0 = 790$ MeV, while four different cases are considered for $\alpha b_0 = 350$ MeV (upper left), $\alpha b_0 = 370$ MeV (upper right), $\alpha b_0 = 400$ MeV (lower left) and $\alpha b_0 = 450$ MeV (lower right). The gray shaded areas indicate the density region of coexistence of the broken and restored phases of chiral symmetry. It is evident that the mixed phase shrinks and the chiral phase transition weakens for higher values of the α parameter.

			m_0 [MeV]			
			790	800	820	840
αb_0 [MeV]	Y_{p+}	ρ_B [ρ_0]	M [M_\odot]			
350	13.0%	1.41	1.12	1.09	1.04	1.01
370	13.2%	1.66	1.24	1.20	1.14	1.08
400	13.4%	2.08	1.41	1.38	1.27	1.16
450	13.5%	2.51	1.58	1.53	1.41	1.29

TABLE II. The critical values of the proton fraction for the direct URCA process and corresponding net-baryon number densities and the neutron star masses.

B. Direct URCA process

The direct URCA (DU) process, $n_+ \rightarrow p_+ + e + \bar{\nu}_e$, is essential for the cooling of neutron stars and is not expected to occur in neutron stars with masses of the order of $1 - 1.5 M_\odot$ [45]. When triggered, it leads to a substantial enhancement of the neutrino emission, and hence to the neutron star cooling rates. The DU process becomes operative when a critical value of the proton fraction is exceeded [46]. Taking into account the presence of the parity doublers, as well as assuming that below the deconfinement transition quarks are not populated, the proton fraction is given by

$$Y_{p+} = \frac{\rho_B^{p+}}{\rho_B} = \frac{\rho_B^{p+}}{\rho_B^{p+} + \rho_B^{p-} + \rho_B^{n+} + \rho_B^{p-}}. \quad (17)$$

In general, Y_{p+} can be estimated through the momentum conservation condition for the DU process, assuming quasi-equilibrium, $f_{n_+} \leq f_{p_+} + f_e$, where f_x 's are the Fermi momenta of neutron, proton and electron, respectively [45].

The critical values of masses for the DU process are marked on the mass-radius profiles in Fig. 4 as diamonds. Also shown is the binary-radio-pulsar mass region $M = 1.35(4) M_\odot$ [41] (lower blue band), which sets a lower-bound constraint for the DU threshold in neutron stars. From the figure, it is clear that the DU process becomes operative still in the chirally broken phase, irrespective of the choice of the m_0 and α parameters.

Before the chiral transition takes place, the parity partners of proton and neutron are not populated, i.e., their densities are zero. The only relevant degrees of freedom are the positive-parity groundstate nucleons and leptons. Hence, in the chirally broken phase, the situation is similar to the case of ordinary nuclear matter. In that case, the critical value for the proton fraction can be deduced [45],

$$Y_{p+}^{\text{DU}} = \frac{1}{1 + (1 + \sqrt[3]{Y_e})^3}, \quad (18)$$

where $Y_e = \rho_e/(\rho_e + \rho_\mu)$. The ρ_e and ρ_μ are the electron and muon densities. Y_e may vary from 1/2 ($\rho_e = \rho_\mu$)

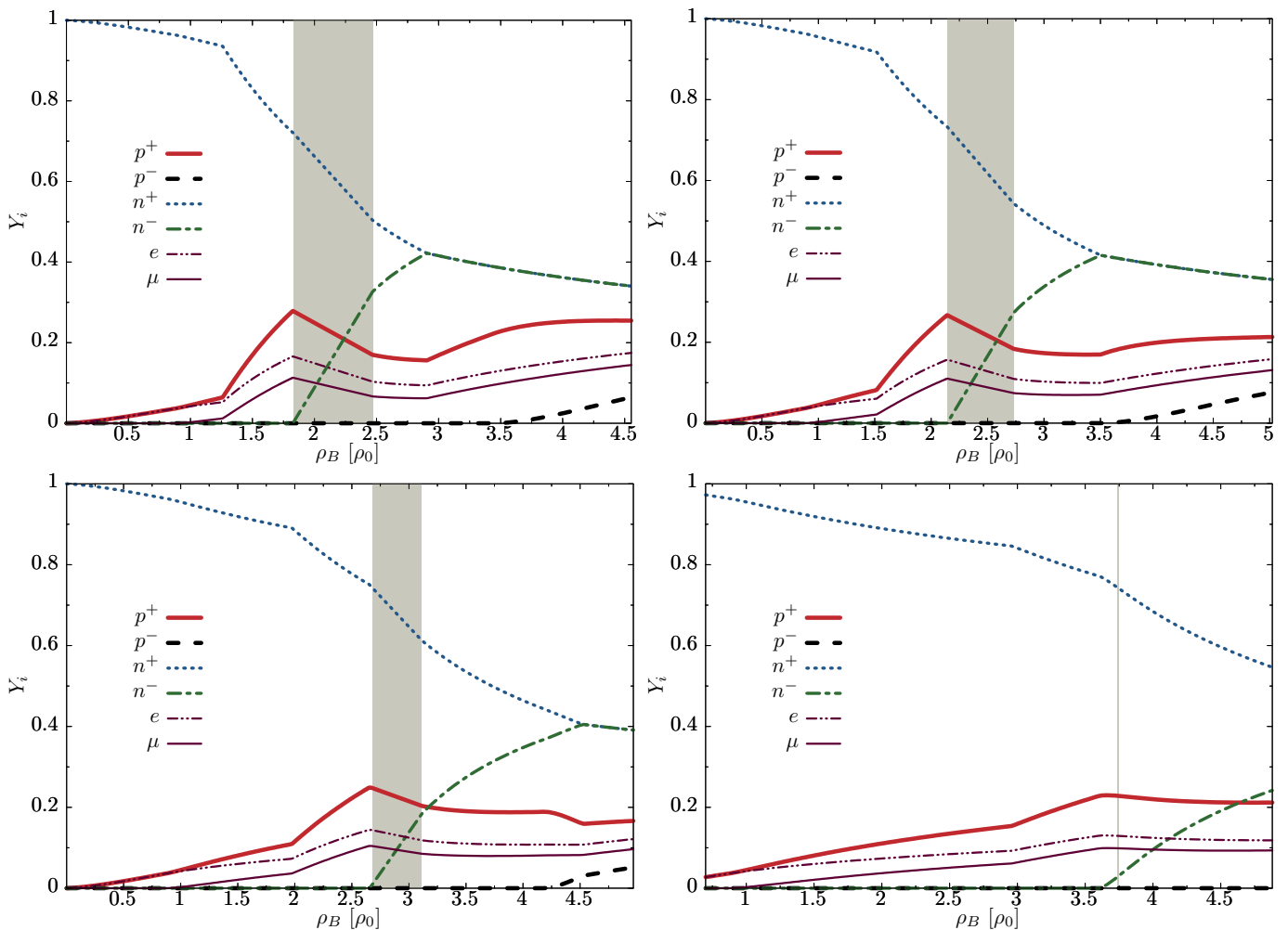


FIG. 6. Composition of compact star matter as a function of the baryon density for the present model. The chirally invariant baryon mass is fixed to $m_0 = 790$ MeV, while four different cases are considered for $\alpha b_0 = 350$ MeV (upper left), $\alpha b_0 = 370$ MeV (upper right), $\alpha b_0 = 400$ MeV (lower left), and $\alpha b_0 = 450$ MeV (lower right). The gray shaded area indicate the density regions of coexistence of the broken and restored phases of chiral symmetry.

to 1 ($\rho_\mu = 0$). We indicate this range in Fig. 7 (green bands). For $Y_e = 1/2$, the critical value is 14.8%, and it goes down to 11.1% for the muon-free case.

The above estimate changes when the negative-parity chiral partners are populated. To see this, let us assume a phase with fully restored chiral symmetry. In this limit, we expect that the parity doublers are degenerate, hence their densities are equal. The charge neutrality condition becomes $2\rho_{p^+} = \rho_e + \rho_\mu$, while the momentum conservation condition remains the same [46], because only the positive parity states take part in the DU process. This might be modified due to the fact that neutrinos have a finite rest mass which results in a mixing of the left and right handed neutrino sectors. In the present work we are not going to elaborate on this interesting beyond-the-standard-model aspect, for which to best of our knowledge at present no investigation exists in the

literature. With this, one finds the threshold to be equal

$$Y_{p^+}^{\text{DU}} = \frac{1}{1 + (1 + \sqrt[3]{2Y_e})^3}. \quad (19)$$

We show this dependence in Fig. 7 (blue bands). For $Y_e = 1/2$, the critical value is 11.1%, and it goes down to 8.0% for the muon-free case. Note that this estimate is systematically lower than the one from Eq. (18).

Also, in Fig. 7, we show two cases calculated for $m_0 = 790$ MeV, namely $\alpha b_0 = 350$ MeV (bottom panel) and $\alpha b_0 = 450$ MeV (top panel). As expected, the critical proton fraction is reached already in the chirally broken phase. The diamonds on the lines indicate net-baryon densities, starting with $1.5 \rho_0$ from the RHS, with a step of $0.5 \rho_0$. From this, it is clear that, while the direct URCA process is always operative in the chirally restored phase at high densities (and thus high star masses), for the case $\alpha b_0 = 350$ MeV it becomes operative already in

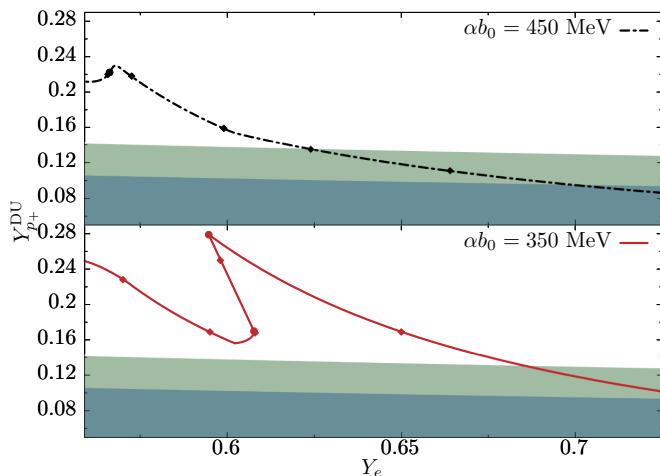


FIG. 7. Proton fraction vs. electron fraction under β -equilibrium and charge neutrality in the hybrid QMN model for $m_0 = 790$ MeV and two extreme values of $\alpha b_0 = 450$ MeV (upper panel) and $\alpha b_0 = 350$ MeV (lower panel). The circles indicate the onset and the restoration of chiral symmetry. The diamonds on the lines indicate densities $\rho_B/\rho_0 = 1.5, 2.0, 2.5, 3.0$ and 3.5 (from the RHS), while the filled circles indicate the onset and end of the chiral restoration transition. The upper gray band shows the region where the direct URCA process is excluded in the case with broken chiral symmetry, while the lower blue band in the case with restored chiral symmetry (see text).

the chirally broken phase at rather low densities in stars of the typical mass range, so that this parametrization becomes highly unfavorable.

In Table II, we show the obtained threshold values of the proton fraction, the corresponding net-baryon number densities and neutron star masses for different values of the chirally invariant mass m_0 and parameter α . Interestingly, we find that the proton fractions, as well as corresponding net-baryon densities, practically do not depend on the parameter. On the other hand, the neutron star masses, at which the threshold is reached, decrease with increasing m_0 and decreasing αb_0 . This is due to the fact that with lower αb_0 the equation of state becomes stiffer, and hence protons are excited more readily at lower values of the net-baryon density. Similarly, the critical value of neutron star mass shifts towards lower values.

While Eq. (18) provides a very useful estimate for the DU threshold in the chirally broken phase, the estimate given by Eq. (19) should be taken with caution. In the current approach, with two sequential phase transitions, the densities, where the parity doublers are fully degenerate, might be beyond the deconfinement transition. Hence, such scenario would not occur. The situation is similar if the two transitions were simultaneous. In such case, the chiral symmetry restoration is accompanied by the transition from hadrons to quarks.

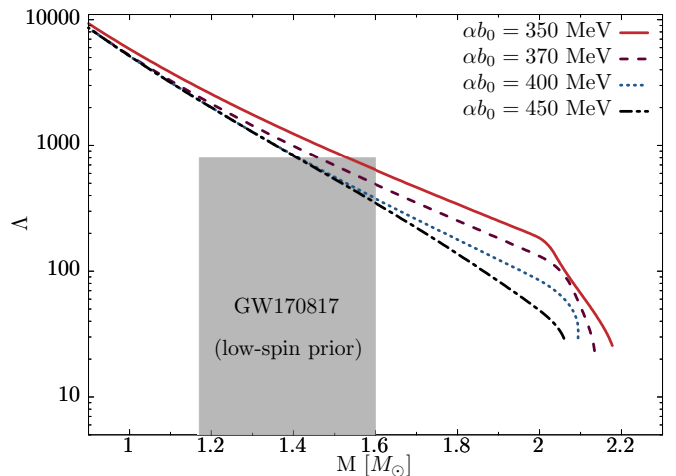


FIG. 8. Top: Tidal deformability parameter Λ as a function of neutron star mass. The gray box shows the $\Lambda < 800$ constraint in the range $1.16 - 1.60 M_\odot$ of the low-spin prior [14].

C. Tidal deformability

The dimensionless tidal deformability parameter Λ can be computed through its relation to the Love number k_2 [47–51],

$$\Lambda = \frac{2}{3} k_2 C^{-5}, \quad (20)$$

where $C = M/R$ is the star compactness parameter, with M and R being the total mass and radius of a star. The Love number k_2 reads

$$k_2 = \frac{8C^5}{5} (1 - 2C)^2 [2 + 2C(y - 1) - y] \times \\ \times \left(2C [6 - 3y + 3C(5y - 8)] \right. \\ \left. + 4C^3 [13 - 11y + C(3y - 2) + 2C^2(1 + y)] \right. \\ \left. + 3(1 - 2C)^2 [2 - y + 2C(y - 1) \ln(1 - 2C)] \right)^{-1}, \quad (21)$$

where $y = R\beta(R)/H(R)$. The functions $H(r)$, and $\beta(r)$ are given by the following set of differential equations,

$$\frac{d\beta}{dr} = 2 \left(1 - 2 \frac{M(r)}{r} \right)^{-1} \\ H \left\{ -2\pi \left[5\epsilon(r) + 9P(r) + \frac{d\epsilon}{dp}(\epsilon(r) + P(r)) \right] \right. \\ \left. + \frac{3}{r^2} + 2 \left(1 - 2 \frac{M(r)}{r} \right)^{-1} \left(\frac{M(r)}{r^2} + 4\pi r P(r) \right)^2 \right\} \\ + \frac{2\beta}{r} \left(1 - 2 \frac{M(r)}{r} \right)^{-1} \\ \left\{ \frac{M(r)}{r} + 2\pi r^2 (\epsilon(r) - P(r)) - 1 \right\}, \quad (22)$$

$$\frac{dH}{dr} = \beta. \quad (23)$$

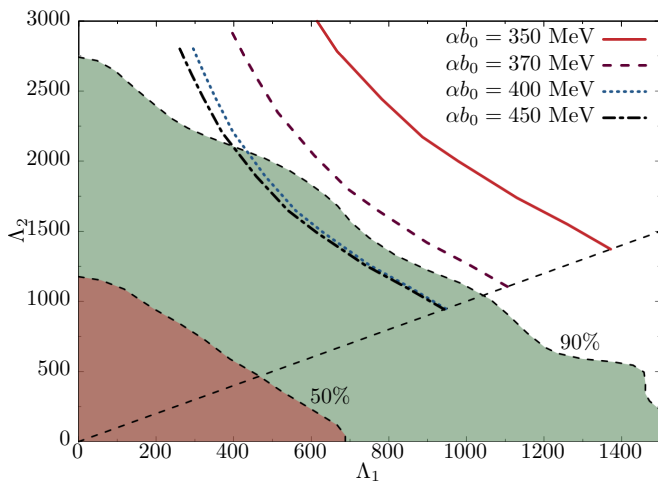


FIG. 9. Tidal deformability parameters Λ_1 and Λ_2 of the low- and high-mass mergers obtained from $\Lambda(m)$ relation for $m_0 = 790$ MeV. Shown are also the 50% and 90% probability contours for the low-spin prior [14].

The above equations have to be solved along with the TOV equations (16). The initial conditions are $H(r \rightarrow 0) = c_0 r^2$ and $\beta(r \rightarrow 0) = 2c_0 r$, where c_0 is a constant, which is irrelevant in the expression for the Love number k_2 .

In Fig. 8, we show the dimensionless tidal deformability parameter Λ as a function of neutron star mass M , for $m_0 = 790$ MeV. We also show the constraint derived in [14], $\Lambda(1.4 M_\odot) < 800$. The constraint is met only for the cases with $\alpha b_0 = 400$ and 450 MeV. In Fig. 9, we plot the tidal deformability parameters Λ_1 vs. Λ_2 of the high- and low-mass members of the binary merger together with the 50% and 90% fidelity regions obtained by the LVC analysis of the GW170817 merger event [14]. We note that, similarly to the direct URCA constraint, the tidal deformability parameter favors soft equations of state. Hence, the tidal deformability can be used to further constrain the range of model parameters m_0 and αb_0 . We discuss this matter in the next subsection.

D. Isospin-symmetric QCD phase diagram

The observational neutron-star data provide useful constraints on the structure of strongly interacting matter. Furthermore, they may constrain the phase diagram of isospin-symmetric QCD matter, which is of major relevance for the heavy-ion physics.

In Fig. 10, we compile the three constraints discussed in this work in the $(\alpha b_0, m_0)$ -plane. Firstly, we show the constraint on the maximum mass of non-rotating, cold neutron stars (red solid line), namely

$$2.01 < M/M_\odot < 2.16. \quad (24)$$

Its lower limit is derived by accurate observations of mas-

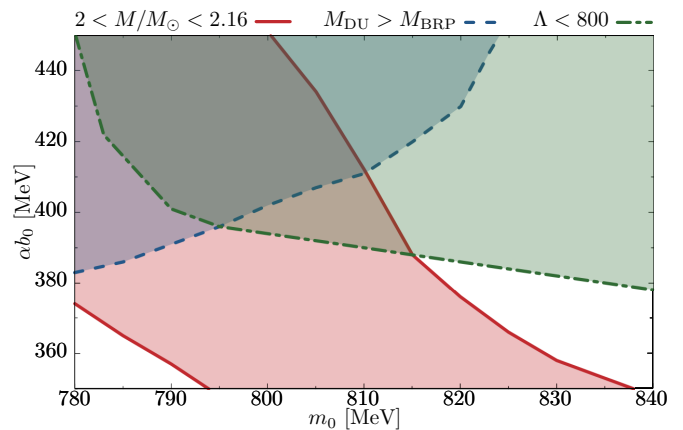


FIG. 10. Constraints for the model parameters m_0 and αb_0 : The maximum mass constraint (red solid line); the direct URCA (blue dashed line); the tidal deformability constraint (green broken-dashed line). The corresponding shaded areas show regions where the constraints are met (See text for details).

sive pulsars in binary systems [13]. The upper limit, on the other hand, was deduced from the assumption that the GW170817 merger event could not have collapsed directly into a black hole, but rather formed a super massive and rapidly-rotating neutron star [52, 53]. We note that similar upper limit on the maximum mass was derived independently in Refs. [54, 55]. Secondly, we show the lower bound for the mass of a star in which the direct URCA process becomes operable (blue dashed line). This constraint is that the direct URCA process should not be operable in neutron stars with mass below the mass of the binary radio pulsar, $M_{\text{BRP}} \approx 1.4 M_\odot$. Finally, the constraint on the tidal deformability parameter, $\Lambda(1.4 M_\odot) < 800$, induced from the GW170817 merger event analysis [14] is shown as the green broken-dashed line. The areas with corresponding shaded colors show regions where the constraints are met. The region where they overlap gives the most preferable sets of the external parameters αb_0 and m_0 . We note that, by construction, the allowed range for αb_0 is roughly $300 - 450$ MeV [11, 12]. Since higher m_0 , in general, yields softer equation of state, the stiffness required by the maximum mass constraint is compensated by lower values of αb_0 , and inversely for the remaining two constraints. At lower values of m_0 , the maximum mass constraint is met practically for the whole range of αb_0 , and the region of overlap is set by the other two constraints (top left corner of the figure). Hence, in general higher values of αb_0 are more preferable. The three constraints are met down to roughly $m_0 = 780$ MeV. This sets the lower and upper bounds for the m_0 parameter. As a result, the allowed range for m_0 is roughly $m_0 = 780 - 810$ MeV. In Fig. 11, we show the model prediction of the phase diagram in the (T, μ_B) -plane, for the case of $m_0 = 790$ MeV. The first-order liquid-gas

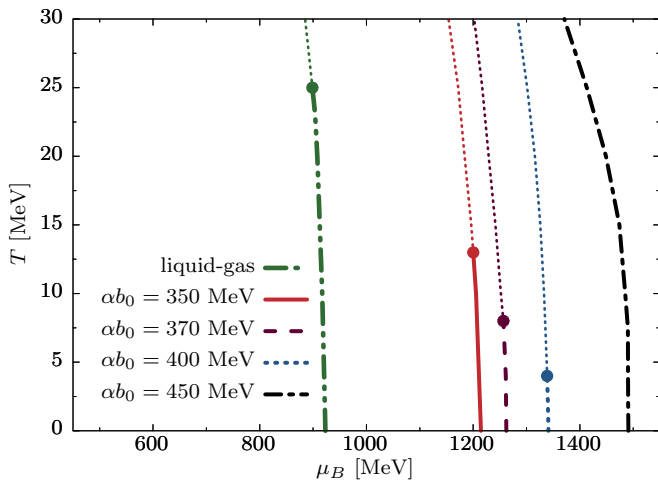


FIG. 11. Low-temperature part of the QCD phase diagram in the (T, μ_B) -plane for isospin-symmetric matter obtained in the hybrid QMN model. The green dashed-doubly-dotted curve corresponds to the liquid-gas phase transition common for all αb_0 . The circles indicate critical points on the transition lines above which, the first-order transition turns into a crossover. No critical point is shown for the case with $\alpha b_0 = 450$ MeV, for which the chiral transition is a smooth crossover at all temperatures.

phase transition (green dashed-doubly-dotted line) develops a critical point around $T = 25$ MeV, and turns into a crossover above it, similarly to the pure parity doublet model. We note that by construction of the hybrid QMN model, the liquid-gas phase transition line is common for all values of the α parameter [11, 12]. Similar phase structure is seen in the chiral phase transition for $\alpha b_0 = 350, 370, 400$ MeV, which develop critical points at $T = 13, 8, 4$ MeV, respectively. On the other hand, for $\alpha b_0 = 450$ MeV, the chiral transition is a smooth crossover at all temperatures. Note that, in view of the constraints discussed in this work (see Sec. IV), the scenarios with $\alpha b_0 = 350$ MeV and $\alpha b_0 = 370$ MeV are rather excluded. Hence, either rather low temperature for the critical endpoint or even its absence in the QCD phase diagram for isospin-symmetric matter is favored.

V. CONCLUSIONS

In this work, we investigated the consequences of a recently developed hybrid quark-meson-nucleon (QMN) model for the equation of state of dense matter under neutron star conditions and the phenomenology of compact stars. In particular, we focused on the implications of the realization of the chiral symmetry restoration by parity doubling within the hadronic phase. We have demonstrated that a strong first-order phase transition invalidates the implication that a flattening, eventually even occurrence of a mass-twin phenomenon, of the mass-radius relation for compact stars at $2 M_\odot$,

could inevitably signal a deconfinement phase transition in compact stars [9]. We have explored different scenarios for high-mass neutron stars with masses in the range of $2 M_\odot$. We have shown that, within the hybrid QMN model, the high-mass stars, such as the PSR J0348+0432 pulsar with the mass $2.01(4) M_\odot$ [13], can be realized in different ways. First, as a neutron star with single-phase nuclear matter with broken chiral symmetry. Second, where its core is made of a mixed phase surrounded by chirally broken and confined nuclear matter. Finally, as a two-phase nuclear matter star, where the core with chiral symmetry restored but still confined matter is surrounded by a chirally broken and confined phase.

We emphasize that an abrupt change in a mass-radius profile in the high-mass part of the sequence is, in general, a result of a phase transition. As we have shown in this work, in a model with two sequential transitions, it does not need to be associated with the deconfinement transition, and hence does not imply the existence of quark matter in the core of a neutron star. We discussed the dependence of the interior composition on the variation of the model parameter m_0 , which has implications on the mass of the star for which the direct URCA process sets in, as well as on the compactness of the star.

We have discussed how modern astrophysical constraints compiled together allow for better determination of the available parameter range, and demonstrated that not only too soft (excluded by the maximum mass constraint), but also too stiff (excluded by either the direct URCA or the tidal deformability constraint) equations of state may be ruled out in the current approach. Finally, we have shown that, due to the parity doubling phenomenon, the obtained results predict rather low value of the temperature for the critical endpoint of the first-order chiral phase transition in the QCD phase diagram, which eventually may even be absent.

In view of the recent formulation of the three-flavor parity doubling [34, 56] and further lattice QCD studies [25, 26], where it was found that to large extent the phenomenon occurs also in the hyperon channels, it would be of great interest to establish equations of state that include these degrees of freedom. In the current approach, the repulsive vector interaction, as well as the isospin-coupling to the quark degrees of freedom are not taken into account. However, we note that they may be essential for establishing the branch of stable hybrid star solutions. We leave these interesting issues as a matter of future studies.

ACKNOWLEDGMENTS

MM acknowledges comments and fruitful discussions with N.-U. F. Bastian, D. E. Alvarez-Castillo, T. Fischer and M. Szymański. This work was partly supported by the Polish National Science Center (NCN), under Maestro grant no. DEC-2013/10/A/ST2/00106 (KR and CS), Opus grant no. UMO-2014/13/B/ST9/02621

(MM and DB), and Preludium grant no. UMO-2017/27/N/ST2/01973 (MM). DB is grateful for support within the MEPhI Academic Excellence programme

under contract no. 02.a03.21.0005. We acknowledge the COST Actions CA15213 THOR and CA16214 "PHAROS" for supporting networking activities.

-
- [1] L. Lindblom, *Phys. Rev. D* **58**, 024008 (1998) doi:10.1103/PhysRevD.58.024008 [gr-qc/9802072].
- [2] R. C. Tolman, *Phys. Rev.* **55**, 364 (1939). doi:10.1103/PhysRev.55.364
- [3] J. R. Oppenheimer and G. M. Volkoff, *Phys. Rev.* **55**, 374 (1939). doi:10.1103/PhysRev.55.374
- [4] A. W. Steiner, J. M. Lattimer and E. F. Brown, *Astrophys. J.* **722**, 33 (2010) doi:10.1088/0004-637X/722/1/33 [arXiv:1005.0811 [astro-ph.HE]].
- [5] A. W. Steiner, J. M. Lattimer and E. F. Brown, *Astrophys. J.* **765**, L5 (2013) doi:10.1088/2041-8205/765/1/L5 [arXiv:1205.6871 [nucl-th]].
- [6] D. Alvarez-Castillo, A. Ayriyan, S. Benic, D. Blaschke, H. Grigorian and S. Typel, *Eur. Phys. J. A* **52**, no. 3, 69 (2016).
- [7] A. Bazavov *et al.* [HotQCD Collaboration], *Phys. Rev. D* **90**, 094503 (2014) doi:10.1103/PhysRevD.90.094503 [arXiv:1407.6387 [hep-lat]].
- [8] M. G. Alford, S. Han and M. Prakash, *Phys. Rev. D* **88**, no. 8, 083013 (2013).
- [9] D. Alvarez-Castillo, S. Benic, D. Blaschke, S. Han and S. Typel, *Eur. Phys. J. A* **52**, no. 8, 232 (2016).
- [10] E. E. Kolomeitsev, K. A. Maslov and D. N. Voskresensky, *Nucl. Phys. A* **961**, 106 (2017) doi:10.1016/j.nuclphysa.2017.02.004 [arXiv:1610.09746 [nucl-th]].
- [11] S. Benic, I. Mishustin and C. Sasaki, *Phys. Rev. D* **91**, no. 12, 125034 (2015) doi:10.1103/PhysRevD.91.125034 [arXiv:1502.05969 [hep-ph]].
- [12] M. Marczenko and C. Sasaki, *Phys. Rev. D* **97**, no. 3, 036011 (2018) doi:10.1103/PhysRevD.97.036011 [arXiv:1711.05521 [hep-ph]].
- [13] J. Antoniadis *et al.*, *Science* **340**, 1233232 (2013) doi:10.1126/science.1233232 [arXiv:1304.6875 [astro-ph.HE]].
- [14] B. P. Abbott *et al.* [LIGO Scientific and Virgo Collaborations], *Phys. Rev. Lett.* **119**, no. 16, 161101 (2017) doi:10.1103/PhysRevLett.119.161101 [arXiv:1710.05832 [gr-qc]].
- [15] E. Annala, T. Gorda, A. Kurkela and A. Vuorinen, *Phys. Rev. Lett.* **120**, no. 17, 172703 (2018) doi:10.1103/PhysRevLett.120.172703 [arXiv:1711.02644 [astro-ph.HE]].
- [16] S. Popov, H. Grigorian and D. Blaschke, *Phys. Rev. C* **74**, 025803 (2006). doi:10.1103/PhysRevC.74.025803 [nucl-th/0512098].
- [17] C. E. Detar and T. Kunihiro, *Phys. Rev. D* **39**, 2805 (1989). doi:10.1103/PhysRevD.39.2805
- [18] D. Jido, T. Hatsuda and T. Kunihiro, *Phys. Rev. Lett.* **84**, 3252 (2000) doi:10.1103/PhysRevLett.84.3252 [hep-ph/9910375].
- [19] D. Jido, M. Oka and A. Hosaka, *Prog. Theor. Phys.* **106**, 873 (2001) doi:10.1143/PTP.106.873 [hep-ph/0110005].
- [20] C. Patrignani *et al.* [Particle Data Group], *Chin. Phys. C* **40**, no. 10, 100001 (2016). doi:10.1088/1674-1137/40/10/100001
- [21] N. K. Glendenning, *Compact Stars, Nuclear Physics, Particle Physics, and General Relativity*, 2nd ed. (Springer-Verlag, New York, 2000).
- [22] V. Paschalidis, K. Yagi, D. Alvarez-Castillo, D. B. Blaschke and A. Sedrakian, *Phys. Rev. D* **97**, no. 8, 084038 (2018) doi:10.1103/PhysRevD.97.084038 [arXiv:1712.00451 [astro-ph.HE]].
- [23] J. M. Lattimer and Y. Lim, *Astrophys. J.* **771**, 51 (2013) doi:10.1088/0004-637X/771/1/51 [arXiv:1203.4286 [nucl-th]].
- [24] D. Zschesche, L. Tolos, J. Schaffner-Bielich and R. D. Pisarski, *Phys. Rev. C* **75**, 055202 (2007) doi:10.1103/PhysRevC.75.055202 [nucl-th/0608044].
- [25] G. Aarts, C. Allton, S. Hands, B. Jger, C. Praki and J. I. Skullerud, *Phys. Rev. D* **92**, no. 1, 014503 (2015) doi:10.1103/PhysRevD.92.014503 [arXiv:1502.03603 [hep-lat]].
- [26] G. Aarts, C. Allton, D. De Boni, S. Hands, B. Jger, C. Praki and J. I. Skullerud, *JHEP* **1706**, 034 (2017) doi:10.1007/JHEP06(2017)034 [arXiv:1703.09246 [hep-lat]].
- [27] T. Hatsuda and M. Prakash, *Phys. Lett. B* **224**, 11 (1989). doi:10.1016/0370-2693(89)91040-X.
- [28] V. Dexheimer, S. Schramm and D. Zschesche, *Phys. Rev. C* **77**, 025803 (2008) doi:10.1103/PhysRevC.77.025803 [arXiv:0710.4192 [nucl-th]].
- [29] V. Dexheimer, G. Pagliara, L. Tolos, J. Schaffner-Bielich and S. Schramm, *Eur. Phys. J. A* **38**, 105 (2008) doi:10.1140/epja/i2008-10652-0 [arXiv:0805.3301 [nucl-th]].
- [30] C. Sasaki and I. Mishustin, *Phys. Rev. C* **82**, 035204 (2010) doi:10.1103/PhysRevC.82.035204 [arXiv:1005.4811 [hep-ph]].
- [31] S. Gallas, F. Giacosa and G. Pagliara, *Nucl. Phys. A* **872**, 13 (2011) doi:10.1016/j.nuclphysa.2011.09.008 [arXiv:1105.5003 [hep-ph]].
- [32] J. Weyrich, N. Strodthoff and L. von Smekal, *Phys. Rev. C* **92**, no. 1, 015214 (2015) doi:10.1103/PhysRevC.92.015214 [arXiv:1504.02697 [nucl-th]].
- [33] V. Dexheimer, J. Steinheimer, R. Negreiros and S. Schramm, *Phys. Rev. C* **87**, no. 1, 015804 (2013) doi:10.1103/PhysRevC.87.015804 [arXiv:1206.3086 [astro-ph.HE]].
- [34] J. Steinheimer, S. Schramm and H. Stocker, *Phys. Rev. C* **84**, 045208 (2011) doi:10.1103/PhysRevC.84.045208 [arXiv:1108.2596 [hep-ph]].
- [35] A. Akmal, V. R. Pandharipande and D. G. Ravenhall, *Phys. Rev. C* **58**, 1804 (1998) doi:10.1103/PhysRevC.58.1804 [nucl-th/9804027].
- [36] K. Hebeler, J. M. Lattimer, C. J. Pethick and A. Schwenk, *Astrophys. J.* **773**, 11 (2013) doi:10.1088/0004-637X/773/1/11 [arXiv:1303.4662 [astro-ph.SR]].
- [37] D. E. Alvarez-Castillo and D. B. Blaschke, *Phys. Rev. C* **96**, no. 4, 045809 (2017)

- doi:10.1103/PhysRevC.96.045809 [arXiv:1703.02681 [nucl-th]].
- [38] M. G. Alford and A. Sedrakian, *Phys. Rev. Lett.* **119**, no. 16, 161104 (2017) doi:10.1103/PhysRevLett.119.161104 [arXiv:1706.01592 [astro-ph.HE]].
- [39] Z. Arzoumanian *et al.*, arXiv:0902.3264 [astro-ph.HE].
- [40] M. C. Miller and F. K. Lamb, *Eur. Phys. J. A* **52**, no. 3, 63 (2016) doi:10.1140/epja/i2016-16063-8 [arXiv:1604.03894 [astro-ph.HE]].
- [41] S. E. Thorsett and D. Chakrabarty, *Astrophys. J.* **512**, 288 (1999) doi:10.1086/306742 [astro-ph/9803260].
- [42] A. Ayriyan, N.-U. Bastian, D. Blaschke, H. Grigorian, K. Maslov and D. N. Voskresensky, *Phys. Rev. C* **97**, no. 4, 045802 (2018).
- [43] M. A. R. Kaltenborn, N. U. F. Bastian and D. B. Blaschke, *Phys. Rev. D* **96**, no. 5, 056024 (2017) doi:10.1103/PhysRevD.96.056024 [arXiv:1701.04400 [astro-ph.HE]].
- [44] A. Bauswein, O. Just, H. T. Janka and N. Stergioulas, *Astrophys. J.* **850**, no. 2, L34 (2017) doi:10.3847/2041-8213/aa9994 [arXiv:1710.06843 [astro-ph.HE]].
- [45] T. Klahn *et al.*, *Phys. Rev. C* **74**, 035802 (2006) doi:10.1103/PhysRevC.74.035802 [nucl-th/0602038].
- [46] J. M. Lattimer, M. Prakash, C. J. Pethick and P. Haensel, *Phys. Rev. Lett.* **66**, 2701 (1991). doi:10.1103/PhysRevLett.66.2701
- [47] T. Hinderer, *Astrophys. J.* **677**, 1216 (2008)
- [48] T. Damour and A. Nagar, *Phys. Rev. D* **80**, 084035 (2009)
- [49] T. Binnington and E. Poisson, *Phys. Rev. D* **80**, 084018 (2009)
- [50] K. Yagi and N. Yunes, *Phys. Rev. D* **88**, no. 2, 023009 (2013)
- [51] T. Hinderer, B. D. Lackey, R. N. Lang and J. S. Read, *Phys. Rev. D* **81**, 123016 (2010)
- [52] L. Rezzolla, E. R. Most and L. R. Weih, *Astrophys. J.* **852**, no. 2, L25 (2018) doi:10.3847/2041-8213/aaa401 [arXiv:1711.00314 [astro-ph.HE]].
- [53] E. R. Most, L. R. Weih, L. Rezzolla and J. Schaffner-Bielich, *Phys. Rev. Lett.* **120** (2018) no.26, 261103 doi:10.1103/PhysRevLett.120.261103 [arXiv:1803.00549 [gr-qc]].
- [54] B. Margalit and B. D. Metzger, *Astrophys. J.* **850**, no. 2, L19 (2017) doi:10.3847/2041-8213/aa991c [arXiv:1710.05938 [astro-ph.HE]].
- [55] M. Shibata, S. Fujibayashi, K. Hotokezaka, K. Kiuchi, K. Kyutoku, Y. Sekiguchi and M. Tanaka, *Phys. Rev. D* **96**, no. 12, 123012 (2017) doi:10.1103/PhysRevD.96.123012 [arXiv:1710.07579 [astro-ph.HE]].
- [56] C. Sasaki, *Nucl. Phys. A* **970**, 388 (2018) doi:10.1016/j.nuclphysa.2018.01.004 [arXiv:1707.05081 [hep-ph]].